A Small-Angle-Scattering Study of the Pore-Orientation Periodicity in Porous Polymer and Carbon Materials

B. J. Olivier

Department of Physics, Oklahoma State University, Stillwater, Oklahoma 74078

R. R. Lagasse* and D. W. Schaefer

Sandia National Laboratories, Albuquerque, New Mexico 87185

J. D. Barnes and G. G. Long

National Institute of Standards and Technology, Gaithersburg, Maryland 20899

Received June 9, 1996; Revised Manuscript Received September 26, 1996[⊗]

ABSTRACT: Absolute-intensity, small-angle X-ray scattering is used to investigate the pore structure of a carbon foam and its corresponding poly(acrylonitrile) foam precursor, both having a concentric band structure of unusually large spacing. The poly(acrylonitrile) foam was prepared from a solidified blend, containing crystallized maleic anhydride, by subliming the crystalline material. The scattering patterns for both foams reveal anisotropy in their pores and identical periodicity in the pore orientation as a function of distance along the radial direction. The period of pore-orientation oscillations, 3.5 mm, is the same as the period of macroscopically-visible bands present on the surface of both the carbon and poly(acrylonitrile) foams. Furthermore, the pore orientations in both samples show the same oscillatory orientation as the maleic anhydride crystals of the blend from which they were derived. The data suggest that a spherulitic orientation of the maleic anhydride crystals in the blend was imprinted on the polymer phase during crystallization.

Introduction

Spherulites are polycrystalline aggregates that possess a radially-symmetric growth about a central nucleus (seed). In addition to a well-defined growth direction, "banded" spherulites display concentric rings (bands) which propagate radially outward from the nucleation point, where tangents to a ring are perpendicular to the direction of growth. These rings can be identified using various scattering techniques including microscopy. The concentric bands typically have a periodic spacing on the order of micrometers, and length scales over which variations in scattered or absorbed radiation can be observed are indicative of the periodic microstructure.

Banded spherulitic crystallization occurs mostly in synthetic polymers[1] although it has also been observed in materials as diverse as organic liquid crystals,[2] glass ceramics,[3] inorganic salts,[4] and low-molecular-weight organic solvents.[5] In all of these materials, the measured band periodicity has not exceeded 100 μm. Our banded spherulites originate from a crystallized blend of maleic anhydride (MA) and poly(acrylonitrile) (PAN).[6] The blend displays an exceptionally large band spacing, compared to the systems mentioned above. The sublimation of the MA leaves behind a PAN monolith which, upon subsequent pyrolysis, produces a carbon foam. The PAN and carbon foams which we will discuss here are also exceptional in comparison to those systems reported above because they display band spacing over distances on the order of millimeters which are visible to the eye. This large band spacing is unique and it permits the use of small-angle X-ray scattering (SAXS) to resolve the void structure in these materials. To resolve spatial variation in microstructure by SAXS, the beam diameter (0.5 mm in our case) must be smaller than the dimension over which the structural variation occurs. The exceptionally large band spacing within our materials (∼3.5 mm) therefore makes SAXS viable for resolving the underlying change in microstructure causing the visible bands. Besides the large spacing, another unusual feature of the banded structure in the PAN and carbon foams is that crystallinity, required for formation of most banded spherulites, is very low in the former material and totally absent in the latter.

A model describing the origin of the banded appearance in the PAN/MA blend has recently been proposed.[6] Briefly, wide-angle X-ray scattering techniques were used to determine the spatial orientation of the MA unit cells within the blend. The concentric rings in the crystallized blend were attributed to periodic fluctuations in the orientations of MA unit cells as a function of their position along the radial (growth) direction. Furthermore, evidence supporting this "twisting" phenomenon in the PAN/MA blend could be qualitatively deduced by visual observation of a flat surface of the sample.[6] By tilting the sample about the radial growth direction, one observes displacements in the bands with respect to a fixed point. The band displacements are known to be a signature of rotating crystal orientations in banded spherulites.[1] Surprisingly, this same band displacement phenomenon occurs in our carbon sample yet no MA crystals are present. In an analogous way, we hypothesize that the band displacement in the foams is caused by a twisting phenomenon in its microstructure. Below, we present experimental evidence supporting our conjecture.

In this paper we investigate, using SAXS, the relationship between the periodic banded structure in the previously studied crystallized PAN/MA blend and (1) a porous polymer monolith produced by sublimation of the MA and (2) a carbon monolith produced by pyrolyzing the PAN foam. Our data clearly show that the voids present in both foams have an anisotropic shape. Further investigation of the SAXS data suggests that

* To whom correspondence should be sent (Email: rrlagas@sandia.gov).

[⊗] Abstract published in *Advance ACS Abstracts,* November 1, 1996.

S0024-9297(95)00811-4 CCC: $12.00

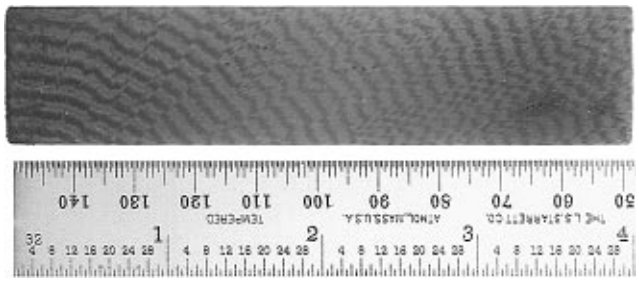

Figure 1. Photograph of a machined surface of the carbon foam showing concentric bands having a period of about 3.5 mm.

the orientation of these anisotropic voids oscillates with a spatial period equal to the spacing of the macroscopically-visible bands found in both foam monoliths. Also, the proposed pore oscillations are found to agree with the spacing of the unit cell rotations previously measured in the crystallized PAN/MA blend.[6] The agreement between the unit cell orientation periodicity and the void periodicity of these materials suggests that the original orientations of the MA crystals are imprinted on the polymer phase of the blend. Finally, our results show that the specific surface areas of the pores, as measured using SAXS, are in good agreement with independent BET nitrogen adsorption measurements.

Experiment

The porous polymer and carbon monoliths were prepared via a three-step process. First, a crystallized poly(acrylonitrile)/maleic anhydride blend was prepared by cooling a 2% wt solution of the polymer from 162 °C to ambient temperature. The maleic anhydride crystallized during the cooling. Second, the maleic anhydride component within the crystallized blend was removed by vacuum sublimation at about 40 °C. The porous polymer residue (foam) was in the form of a foam monolith having dimensions approximately equal to those of the crystallized blend. The mass density of the monolith was $\rho_{PAN} = 33.0$ mg/cm^3, corresponding to a void fraction of 97 vol %. Third, the PAN foam having atomic composition C_3H_3N was heated first in air at 220 °C and then in argon at 1100 °C to produce a microcellular carbon foam.[7] The carbon monolith had a mass density $\rho_{carbon} = 45.2$ mg/cm^3 and a void fraction of 98 vol %.

Figure 1 is a photograph of the carbon monolith. Although a pattern of concentric rings is clearly visible in the carbon structure, it was only faintly visible in the PAN precursor. An average spacing between successive dark bands on the carbon surface is approximately 3.5 mm. The PAN and carbon foams used in the SAXS experiments were rectangular with dimensions $t = 2.1$ mm by $h = 30$ mm by $w = 5$ mm, where t is the sample thickness along the X-ray beam direction.

For the SAXS experiments, we have utilized both the National Institute of Standards and Technology (NIST) double-crystal diffractometer at the National Synchrotron Light Source (NSLS) and a 10-m-long pinhole camera in the NIST Polymer Division. Detailed characteristics of both instruments may be found elsewhere.[8-10]

The double-crystal diffractometer was used to determine absolute differential scattering cross-sections per unit sample volume, $d\Sigma(Q)/d\Omega$. In addition, these measurements, from which specific surface areas were derived, provided an independent check on the surface areas we derived from the pinhole camera using a secondary standard to calibrate intensity, as described below. The NIST double-crystal diffractometer at the NSLS uses a photodiode detector which can measure the intensity of both the incident and the scattered X-ray beam. This permits absolute calibration of the scattered radiation without the need for a secondary standard and without the use of attenuating filters. Unfortunately, only the carbon foam was available at the time the double-crystal diffractometer was available to us. However, the carbon

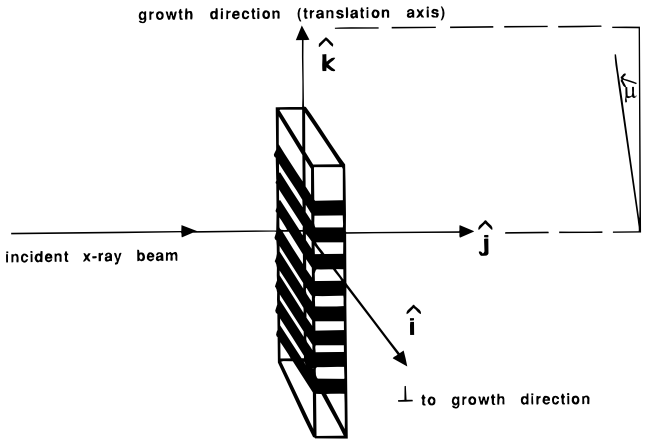

Figure 2. Scattering geometry where $\hat{k}$ is the radial axis which is parallel to the growth direction of MA crystals in the original blend. The beam propagates along $\hat{j}$, and $\hat{i}$ is parallel to the detector plane. The scattering geometry remains fixed in space.

results were in good agreement with the results from the pinhole instrument, so experimental reproducibility between SAXS instruments was verified.

The carbon sample measured with the double-crystal diffractometer was mounted on an aluminum washer, and the incident synchrotron radiation was collimated down to a l mm diameter. Two scattering patterns were measured at different positions along the growth axis. First, data were recorded with the synchrotron X-ray beam incident directly on a dark band, and then for the incident beam centered between two adjacent dark bands (see Figures 1 and 2).

A 10-m-long pinhole SAXS camera on a rotating-anode X-ray source was used to obtain detailed information concerning the pore orientation in the PAN and carbon foams. The measurements involved translating the samples along their growth axes at 0.5 mm increments, using a computer-controlled stepping motor. The scattering patterns were recorded as a function of position. The scattering geometry and sample orientation are sketched in Figure 2. The beam was collimated by a 0.5-mm pinhole placed immediately in front of the sample. The pinhole diameter was only a fraction (15%) of the measured spacing between the bands in each material, and therefore significant structural changes could be observed. From Figure 2, one can see that the incident beam traveled along the $\hat{j}$ direction. Both the $\hat{i}$ and the $\hat{j}$ directions were defined perpendicular to the radial growth direction, $\hat{k}$, for each sample. The $\hat{i}$, $\hat{j}$, and $\hat{k}$ directions remain fixed in the frame of the scattering geometry and the azimuthal angle, μ, is the angle defined in the plane of the detector measured relative to $\hat{k}$.

Theory

Small-angle X-ray scattering probes scattered wave vectors Q ranging from 10^{-4} to 10^{-1} Å^{-1}, where the scattered wave vector is defined as $Q = (4\pi/\lambda)\sin(\phi/2)$, λ is wavelength, and ϕ is scattering angle. Scattered intensities reflect a correlation in X-ray scattering length density on length scales $1/Q$ of between 10 and 10^4 Å. For a material consisting of two phases, the macroscopic SAXS cross section is given by[11,12]

$$d\Sigma(Q)/d\Omega = \left(\frac{1}{V_s}\right)\left|\int_{V_s}\Delta\rho(\vec{r})e^{i\vec{Q}\cdot\vec{r}}\,d\vec{r}\right|^2 \qquad (1)$$

where $\Delta\rho$ is the difference in scattering length density between the two phases and V_s is the sample volume.

Structural information may be derived from the asymptotic region of a scattering curve without further assumption.[12] In particular, for a two-phase material

possessing a sharp interface the asymptotic form of the macroscopic cross-section is given by

$$d\Sigma(Q)/d\Omega \rightarrow K_P/Q^4 \qquad \text{as} \qquad Q \rightarrow \infty \tag{2}$$

K_P is the Porod constant, which may be written in terms of the interfacial area per unit volume of porous material by

$$K_P = 2\pi(\Delta\rho)^2(S/V) \tag{3}$$

where S/V is the specific surface area and $\Delta\rho$ is the difference in the X-ray scattering length densities between the two phases. For porous materials consisting of a void and a solid phase, $\Delta\rho$ is approximately equal to the scattering length density of the solid phase. For materials with randomly oriented pores one may rewrite eq 3 in terms of an average chord length within the pore[13] to obtain

$$K_P = 2\pi(\Delta\rho)^2\frac{4\phi_V}{\langle L_V\rangle} \tag{4}$$

$\langle L_v\rangle$ is defined as the average length of randomly-chosen straight paths interconnecting opposite sides of the pore. ϕ_V is the volume fraction of voids, which was previously computed.

For isotropic scatterers, K_P is independent of the azimuthal scattering angle[11] (μ in Figure 2) and eqs 3 and 4 are rigorously true for all two-phase materials which meet the criterion of a sharp interface. The images obtained from a 2-D position-sensitive detector clearly show the presence of anisotropic pores in both our PAN and carbon monoliths (see below), so that K_P depends on the azimuthal scattering angle.

To account for the anisotropy, we adopt the treatment of Hamzeh and Bragg[14] as extended by Wu.[15] The angular dependent Porod constant at the large-Q limit is[15]

$$K_P(\mu) = \frac{2\pi(\Delta\rho)^2(S/V)}{[(e_k\cos\mu)^2 + (e_i\sin\mu)^2]^2} \tag{5a}$$

where we have made the assumption that the anisotropic pores can be generated from *equivalent volume* spherical pores by stretching or shrinking along three orthogonal axes which define the orientation of the anisotropic pore. The $\vec{e}_x$ s are the elongation axes whose magnitudes quantify the amount of stretching or shrinking required to produce anisotropic pores, as illustrated in Figure 3. We remark that the pore shapes in Figure 3 do not reflect the true shape of the voids in our foams. We have chosen ellipsoids as an idealization of the pore shape. The requirement for equal pore volume introduces the constraint $(e_ie_je_k)^{1/3} = 1$. We assume that one of the pore elongation axes, $\vec{e}_k$, is parallel to and remains fixed along the $\hat{k}$ direction of the scattering geometry shown in Figure 2. This direction corresponds to the radial crystal growth direction of the original MA blend. The remaining two elongation axes, $\vec{e}_i$ and $\vec{e}_j$, are therefore perpendicular to the growth direction but not fixed with respect to the scattering geometry. The model we develop for the PAN and carbon foams envisions a rotation of the pore elongation axes $\vec{e}_i$ and $\vec{e}_j$ around the $\hat{k}$ axis, as is illustrated in Figure 4b. At a given position in the band structure, $\vec{e}_i$ may be parallel to the transverse $\hat{i}$ scattering direction and eq 5a is valid. At other positions along the growth direction, $\vec{e}_j$ may be parallel to the $\hat{i}$ direction and eq 5a is modified accordingly,

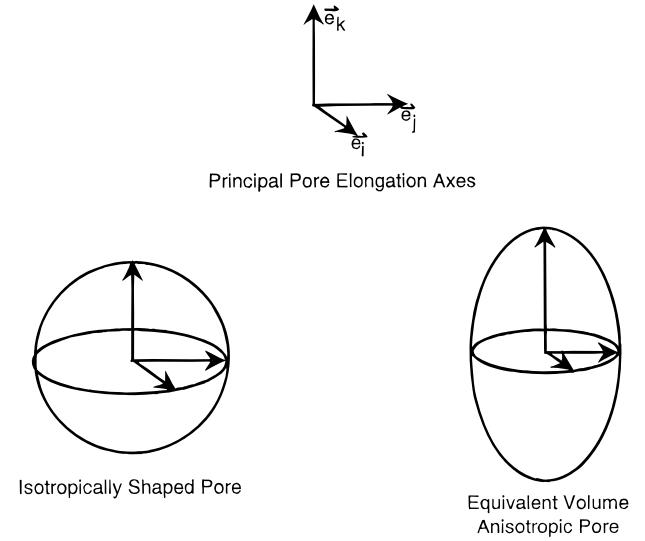

Figure 3. Transformation of an isotropic pore into an equivalent volume anisotropic one. The pore elongation axes are denoted $\vec{e}_i$, $\vec{e}_j$, and $\vec{e}_k$. The $\vec{e}_i$ and $\vec{e}_j$ axes are free to rotate about the axis which defines the direction of the sample translation in the scattering geometry. The lengths of the pore axes correspond to the amount of deformation of the isotropic shape.

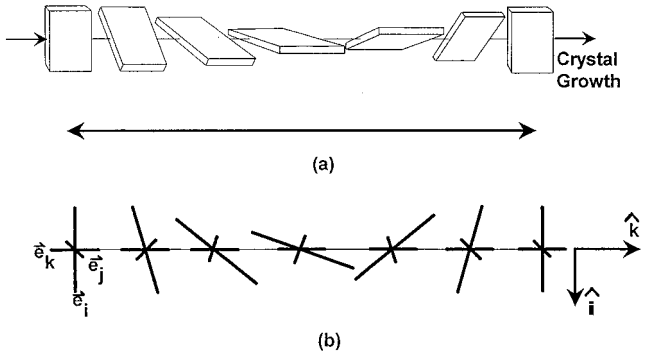

Figure 4. (a) Conceptual illustration of the rotating orientation of MA orthorhombic unit cells. The radial coordinate of the concentric band structure is indicated by the arrow. (b) Rotating elongation axes used to characterize spatially periodic orientation of anisotropic pores. $\vec{e}_k$ is parallel to the radial (growth) direction of crystals in the MA blend.

$$K_P(\mu) = \frac{2\pi(\Delta\rho)^2(S/V)}{[(e_k\cos\mu)^2 + (e_j\sin\mu)^2]^2} \tag{5b}$$

The positions along the growth front where eqs 5a and 5b apply should be separated by half the spatial period of a 360° pore rotation. The rotation of the elongation axes $\vec{e}_i$ and $\vec{e}_j$ is analogous to the earlier proposed model[6] for describing the rotation of the MA unit cells of the PAN/MA blend, as shown in Figure 4a. It is important to note that the specific surface areas (S/V) in eqs 5 correspond to the equivalent volume unstretched isotropic voids. Finally, for the isotropic case, $e_i = e_j = e_k = 1$ and eqs 5 reduce to the equation for isotropic scatterers, eq 3.

Results and Discussion

The results from the double-crystal diffractometer and the pinhole camera are compared in Figure 5 where representative scattering curves from the same carbon

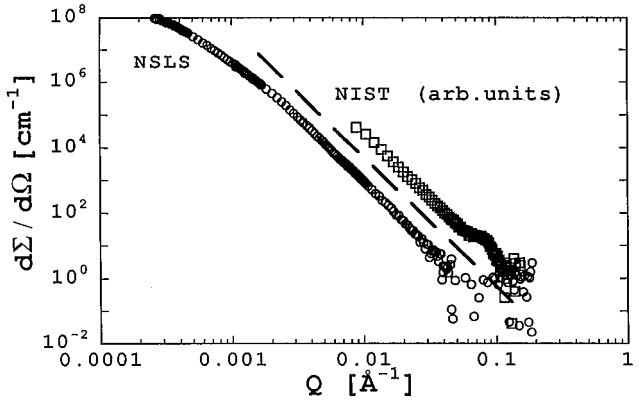

Figure 5. Small-angle scattering curves from the carbon foam. The circles represent measurements taken with the double-crystal diffractometer, which are on an absolute scale. The squares represent measurements from the pinhole camera and were calculated from circularly-averaged intensities, in arbitrary intensity units.

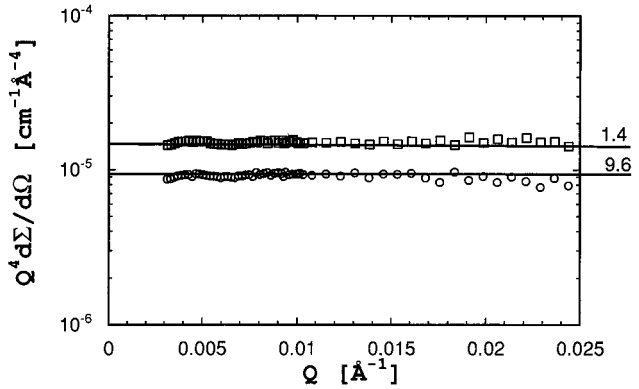

Figure 6. Porod plot calculated from double-crystal diffractometer measurements. The circles show the results when the incident beam was directly incident on a dark band. The squares are the results when the incident beam was positioned between two successive dark bands.

sample are plotted on a log scale. Data from the pinhole camera are a circular average from a typical point on the specimen and are not on an absolute scale. The double-crystal diffractometer data extend 1 order of magnitude lower in Q because of the higher angular resolution provided by the collimation. Both curves exhibit Porod behavior for an extensive range in Q (power-law slope $= -4$), as indicated by the dashed line, suggesting an abrupt polymer−void interface. However, two comments are in order concerning these results. First, a desmearing routine had to be performed on the double-crystal data but not on the pinhole camera data. Desmearing double-crystal slit-smeared data is rigorous for isotropic scatterers only; therefore errors may have been introduced. Our results from the two instruments, however, were consistent with one another, suggesting that the error introduced through desmearing was minimal. The increased intensity in the pinhole camera data, seen at approximately 0.08 $Å^{-1}$, is an artifact which resulted from spurious scatter from a beryllium window positioned at the exit to the scattered beam path, just ahead of the 2-D position-sensitive detector. Fortunately, this artifact will not affect our analysis below. The PAN foam shows analogous Porod behavior over a similar range of Q values.

Figure 6 shows a Porod plot of scattering by the carbon material measured using the double-crystal instrument. For the lower curve, the X-ray beam was incident directly on a dark band. Using eq 6 we

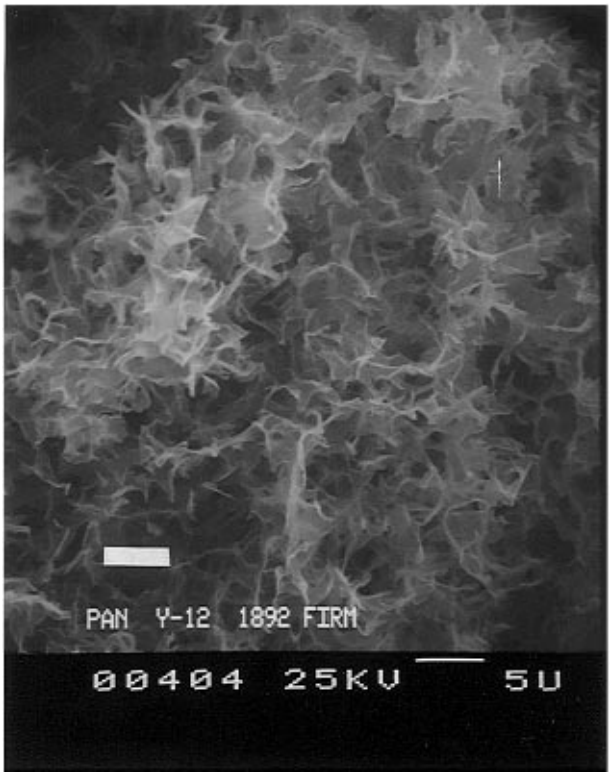

Figure 7. Scanning electron micrograph of a fracture surface of the carbon foam. A 5 μm scale marker is shown.

calculate the specific surface area to be $S/V\rho_{carbon} = 18.3$ m^2/g. For the upper curve, where the X-ray beam was incident between two successive dark bands, we find $S/V\rho_{carbon} = 26.7$ m^2/g. These experimental values do not consider the azimuthal dependence of the scattered intensity. Using eq 4, we calculate average chord lengths within the voids to be $\langle L_V \rangle = 5$ μm for scatter from the dark band and $\langle L_V \rangle = 3$ μm for the scatter between successive dark bands. Average chord lengths in the range of 3 to 5 μm are consistent with the pore structure shown in Figure 7.

The NIST pinhole camera, with its two-dimensional position-sensitive detector, was used to characterize pore orientations in our sample foams. Two data runs were performed on each foam to verify reproducibility. The incident X-ray beam was collimated down to a 0.5-mm diameter. Each run consisted of translating the sample in 0.5-mm increments for a total of 11 mm along the $\hat{k}$ direction, yielding 22 independent scattering patterns.

Two-dimensional difference images of the scattering from the carbon foam are shown in Figure 8. The images were generated by first averaging all 22 scattering patterns and then subtracting individual patterns taken at successive 0.5-mm increments from the averaged image. The distance given beneath each image is the distance measured along the growth axis defined relative to an arbitrary starting point. The individual images clearly display an anisotropic scattering pattern which appears periodic after approximately 3 mm of translation along the $\hat{k}$ direction. The apparent repetition in these scattering patterns becomes more pronounced with the Porod analysis given below. Similar 2-D scattering images were observed in the PAN foam data.

To further quantify the periodic spatial behavior of the anisotropy in the scattering, we performed sector averages for each scattering pattern in order to deter-

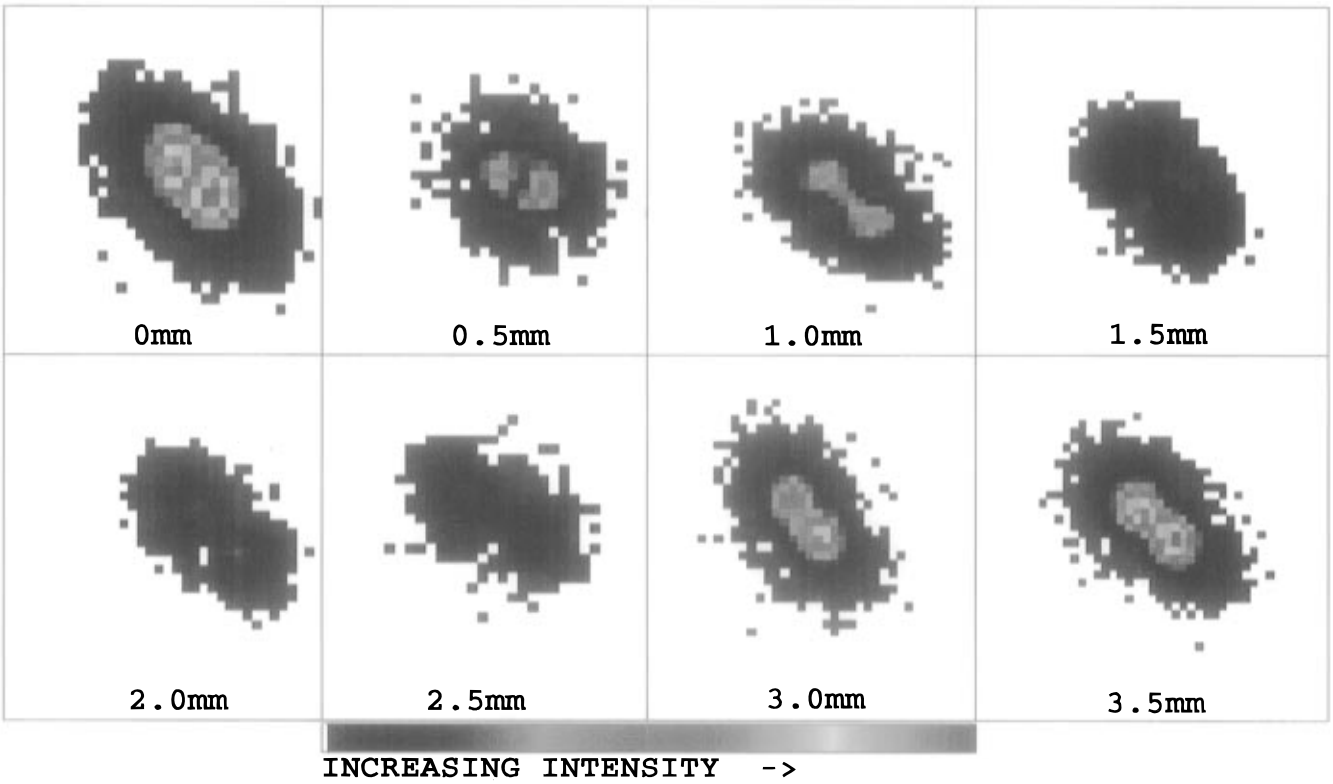

Figure 8. Sequence of 2-D position-sensitive detector images taken over 3.5 mm of translation along the growth axis ($\hat{k}$) of the carbon foam. The images display relative scattered pixel intensities from the pinhole measurements. The growth direction is along a line directed from the lower right corner to the upper left corner for each image.

Figure 9. View of 2-D position-sensitive detector plane, showing the geometry used in the data analysis. The lines show the angular range of the $\langle\mu\rangle = 0°$ and $\langle\mu\rangle = 90°$ sector averages. The scattering pattern is a contour map of the image shown in Figure 8 at $k = 0.5$ mm. The size of the image relative to the area of the detector plane is not to scale.

mine the azimuthal angle dependence of the Porod constant, $K_P(\mu)$. Here $K_P(\mu)$ refers to the Porod constant calculated using the scattered intensity I expressed in arbitrary units, not macroscopic scattering cross section units. (Since this portion of the analysis will eventually lead to computations requiring *ratios* of K_p values, their units are unimportant as long as they are self-consistent.) Sector-averaged intensities were calculated along two directions of the scattering geometry, the growth direction $\hat{k}$ and the direction perpendicular to it along $\hat{\imath}$. Figure 9 shows intensity contours superimposed on the detector plane in order to illustrate the geometry used for calculating these sector averages. $\mu = 0$ is defined along the radial direction $\hat{k}$. In order to

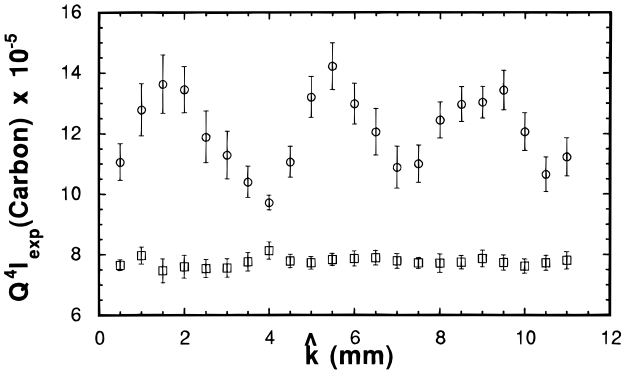

Figure 10. Plot of Q^4I_{exp} versus position along the growth direction for the carbon foam. The top curve represents scattered intensities measured perpendicular to the growth direction, while the bottom curve represents intensities measured parallel to the growth direction. I_{exp} are in arbitrary intensity units, as explained in the text.

determine the behavior of K_P along $\hat{k}$ we calculated the average scattered intensity along an annulus with a given Q value for $-22.5° < \mu < 22.5°$ ($\langle\mu\rangle = 0°$). This averaging was necessary in order to achieve acceptable statistics. In an analogous way, to determine the behavior of K_P along $\hat{\imath}$, a sector average is defined for $67.5° < \mu < 112.5°$ ($\langle\mu\rangle = 90°$). Two-dimensional plots of $Q^4I(Q)$ (with I in arbitrary units) showed that variations in K_p within the sectors are relatively minor. The K_P were then read from plots of $Q^4I(Q)$ vs Q for regions over which the ordinate was reasonably constant.

The K_p values calculated from sector averages along the $\hat{k}$ and $\hat{\imath}$ scattering directions are shown in Figure 10 for the carbon foam sample. Since both carbon foam runs displayed similar behaviors for corresponding sector averages, the runs were averaged in Figure 10. The upper curve represents sector averages along $\hat{\imath}$ as

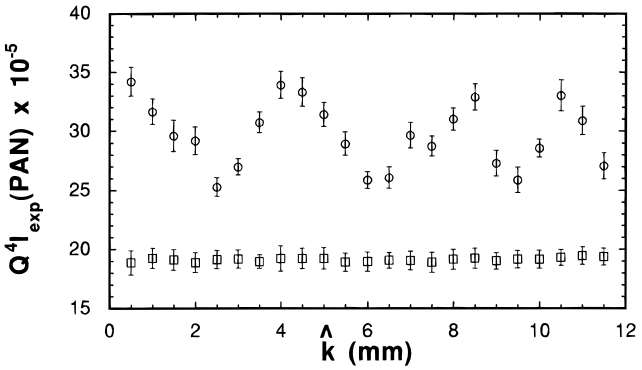

Figure 11. Plot of Q^4I_{exp} for the PAN foam at different positions along the growth axis. The top curve represents intensities measured perpendicular to the growth direction while the bottom line represents intensities measured parallel to the growth direction. I_{exp} are in arbitrary intensity units.

a function of distance traversed along the radial (growth) direction of the sample. The lower shows corresponding sector averages for $\langle\mu\rangle = 0°$ calculated at these same positions. Notice that the values of $K_P(\langle\mu\rangle = 90°)$ oscillate with a period of approximately 3−4 mm. This spatial period in K_P is the same as the spatial period of the visible concentric banding shown in Figure 1. Furthermore, it qualitatively agrees with the periodicity of the 2-D scattering images shown in Figure 8. Conversely, $K_P(\langle\mu\rangle = 0°)$ shows no oscillatory behavior.

Figure 11 shows the corresponding K_p results for two averaged PAN foam runs. Analogous to the carbon foam data, $K_P(\langle\mu\rangle = 90°)$ oscillates while $K_P(\langle\mu\rangle = 0°)$ remains essentially constant, independent of position along the growth direction. The oscillation in K_P for $\langle\mu\rangle = 90°$ and lack of oscillation for $\langle\mu\rangle = 0°$ are key observations. They suggest a rotating model for anisotropic pores, analogous to the case of MA crystals, as illustrated in Figure 4.

Using eq 5a we can quantify the angular dependence of K_P for defined positions along the growth axis. At a given position along $\hat{k}$, the perpendicular Porod constant is given by

$$K_P(\langle\mu\rangle = 90°) = \frac{2\pi(\Delta\rho)^2(S/V)}{e_i^4} \tag{6a}$$

where we have assumed that $\vec{e}_i$ is parallel to $\hat{\imath}$. For this case, K_P is inversely proportional to the fourth power of the elongation ratio e_i. Conversely, for positions displaced half a spatial period from the original position along $\hat{k}$ we have from eq 5b,

$$K_P(\langle\mu\rangle = 90°) = \frac{2\pi(\Delta\rho)^2(S/V)}{e_j^4} \tag{6b}$$

where the pore's elongation axis $\vec{e}_j$ is now parallel to the $\hat{\imath}$ direction of the scattering geometry and K_P is now inversely proportional to the fourth power of the elongation ratio e_j. Because the elongation axis $\vec{e}_k$ remains parallel to $\hat{k}$, either eq 5a or 5b may be used to calculate an expression for the behavior of the Porod constant along the growth direction, i.e.,

$$K_P(\langle\mu\rangle = 0°) = \frac{2\pi(\Delta\rho)^2(S/V)}{e_k^4} \tag{6c}$$

Taking the ratio of eqs 6a and 6c gives an expression for the relative deformation along the axis corresponding to $\vec{e}_i$ as

$$\frac{K_P(\langle\mu\rangle = 0°)}{K_P(\langle\mu\rangle = 90°)} = \left(\frac{e_i}{e_k}\right)^4 \tag{7a}$$

The specific surface area of the equivalent isotropic pore S/V does not appear since it is a constant. The exponent, 4, in eq 7a means that the ratio of the Porod constants is sensitive to small differences between elongation ratios e_i and e_k. Notice that since eq 7a involves a ratio of Porod constants, absolute intensities are not necessary for quantitatively characterizing pore anisotropy.

Taking the ratio of eqs 6b and 6c gives an expression defining the relative deformation along the axis corresponding to $\vec{e}_j$ as

$$\frac{K_P(\langle\mu\rangle = 0°)}{K_P(\langle\mu\rangle = 90°)} = \left(\frac{e_j}{e_k}\right)^4 \tag{7b}$$

Using eqs 7a and 7b, we now analyze the data shown in Figures 10 and 11. First we consider the spatial positions along the growth front of the carbon foam where the Porod constant along the transverse $\hat{\imath}$ reaches a maximum value of approximately 13.5. For these positions along the growth direction, eq 7a yields $e_i = 0.87e_k$. For the positions along $\hat{k}$ where the transverse Porod constant reaches a minimum value of approximately 9.5 we have, from eq 7b, $e_j = 0.944e_k$. To determine the three independent elongation ratios, we use the equivalent volume condition of $(e_ie_je_k)^{1/3} = 1$. From this, we find $e_i = 0.93$, $e_j = 1.00$, and $e_k = 1.07$. Finally, we note that because the deformations are less than 10%, the anisotropy in the pore shape may be too small to be seen in Figure 7.

Corresponding calculations for the PAN foam, using the data from Figure 11 and the equivalent volume condition, yield approximately the same values for e_i, e_j, and e_k (at least to within our experimental accuracy). The anisotropy in the pore shape is, therefore, nearly the same for both materials suggesting that the anisotropy in the pore structure of the PAN foam remains undisturbed during pyrolysis. The e_x values suggest that the crystallization of the MA precursor blend stretches the polymer phase by 7% along the growth direction, compresses by 7% along one of the directions perpendicular to the growth direction, and causes no deformation along the other perpendicular direction. It is interesting to note that the MA crystallization deforms the polymer phase along only one of the two axes perpendicular to the growth axis. It would be interesting to search for corresponding structural anisotropy in phase-separated polymer blends having one spherulitically crystallized component to further investigate this phenomenon.

We are aware of the uncertainties associated with any 2-D model which resulted from a 3-D structure and realize other possibilities may exist for explaining the SAXS data. However, we point out that our model is successful in explaining our experimental results in addition to retaining self-consistency with the previous interpretation of the structure in the precursor blend.

The final part of the results concerns surface area determination using the pinhole SAXS camera and a comparison of these results with those from BET analysis of nitrogen adsorption measurements and with

Table 1. Comparison of Specific Surface Area Measurements Obtained Using the Pinhole Camera and the Double-Crystal SAXS Diffractometer and BET Nitrogen Adsorption[a]

technique	carbon (m^2/g)	PAN (m^2/g)
pinhole SAXS	17.5 ± 4.0	39.5 ± 4.0
double-crystal SAXS	22.5 ± 4.2	not available
BET	13	37

[a] The values following the ± represent the variations between the extreme values of the data.

those derived above from the double-crystal diffractometer measurements. Small-angle pinhole spectrometers usually must be calibrated against a known standard before an absolute scattered intensity can be determined. We converted the NIST pinhole camera results to absolute intensity using standard procedures[16] and a polyethylene standard. The absolute scattering intensity for that standard was measured using the double-crystal diffractometer.

Using the pinhole camera absolute-intensity measurements on the carbon foam, we calculate the lower limit for the perpendicular Porod constant to be $K_P(\langle\mu\rangle = 90°) = 0.92 \times 10^{37}$ m^{-5}. Substituting this value and $e_j = 1.00$ into eq 6b we find $S/V\rho_{carbon} = 17.5$ m^2/g. Recall that the surface area in eqs 6 represents that of an equivalent volume isotropic structure and not the actual anisotropic structure. Since the anisotropy reflected in the elongation ratio is only 7%, the difference between surface areas of the actual anisotropic and equivalent isotropic structures is expected to be small (actually on the order of <1%). Therefore, the calculated value for $S/V\rho_{carbon}$ above is a good estimate of the surface area for the actual anisotropic voids making up our carbon foam. Using the double-crystal diffractometer results we calculate an average surface area of $\langle S/V\rho_{carbon}\rangle = 22.5$ m^2/g. For the PAN foam, absolute intensities derived using the pinhole camera and a secondary standard yield a lower limit to the Porod constant along $\hat{i}$ equal to $K_P(\langle\mu\rangle = 90°) = 2.30 \times 10^{37}$ m^{-5} and a corresponding specific surface area of $S/V\rho_{PAN} = 39.5$ m^2/g.

Surface areas derived from the pinhole camera and the double-crystal diffractometer are compared to the nitrogen adsorption measurements in Table 1. Summarizing, the value calculated from the pinhole camera for the PAN material agrees within experimental error with the BET value. The value calculated for the carbon foam using the pinhole camera is somewhat lower than that found from the double-crystal diffractometer data, but its value is also within our experimental uncertainty. Finally, the surface area for the carbon material, derived from both SAXS instruments, is somewhat higher than the BET measurement. This discrepancy may be explained by assuming that closed pores are present in the carbon structure. Closed pore regions of the carbon foam are inaccessible to nitrogen adsorption at 77 K, yet these pores would be included in the SAXS characterization.

Conclusions

The pore structure of two foams, derived from a large-banded spherulitic poly(acrylonitrile)/maleic anhydride blend, was measured using SAXS. The PAN foam was prepared via sublimation of the crystallized MA from the original blend and the carbon foam was a pyrolyzed version of the PAN. Both monoliths displayed alternating band structures with a spatial period of 3.5 mm, equivalent to the spacing found in the original blend. Our results showed that both porous polymer networks contained anisotropic voids having one of the principal axes fixed along the same growth direction as the MA crystals in the original blend. The SAXS results were consistent with the interpretation of a periodic rotation of the two remaining principal pore axes. The spatial period of rotation, 3−4 mm, was the same for both foams. The rotational period of the pores also agreed with the macroscopically-observed spacing of the concentric bands on machined surfaces of each material. We interpret the bands as being a direct consequence of the pore rotation. The anisotropic pore structures were believed to result from the deformation of the polymer phase during the crystallization of the maleic anhydride in the precursor blend.

Acknowledgment. A. P. Sylwester introduced the authors to the banding phenomenon in the crystallized polymer−solvent precursor and foams. The work at Sandia National Laboratories was supported by the U.S. Department of Energy under contract DE-AC04-94AL85000.

References and Notes

(1) Bassett, D. *Principles of Polymer Morphology*; Cambridge University Press: Cambridge, U.K., 1981.
(2) Adamski, P.; Kazimierski, P. *J. Cryst. Growth* **1984**, *66*, 593.
(3) MacDowell, J. *J. Am. Ceram. Soc.* **1990**, *73*, 2287.
(4) Matsuno, T.; Koishi, M. *J. Cryst. Growth* **1989**, *94*, 798.
(5) George, J.; Premachandran, S. *J. Cryst. Growth* **1979**, *46*, 297.
(6) Lagasse, R. *J. Cryst. Growth* **1994**, *140*, 370.
(7) Sylwester, A.; Aubert, J.; Rand, P.; Arnold, C.; Clough, R. *Polym. Mater. Sci. Eng.* **1987**, *57* (2), 113.
(8) Barnes, J.; Mopsik, F. In *46th Annual Technical Conference Proceedings, Society of Plastic Engineers*; Society of Plastic Engineers: Fairfield, CT, 1988; p 1178.
(9) Hendricks, R. *J. Appl. Crystallogr.* **1978**, *11*, 15.
(10) Long, G.; Jemian, P.; Weertman, J.; Black, D.; Burdette, H.; Spal, R. *J. Appl. Crystallogr.* **1991**, *24*, 30.
(11) Windsor, C. *J. Appl. Crystallogr.* **1988**, *22*, 582.
(12) Porod, G. In *Small Angle X-ray Scattering*; Glatter, O., Kratky, O., Eds.; Academic Press: New York, 1982.
(13) Balta-Calleja, F.; Vonk, C. *X-Ray Scattering of Synthetic Polymers;* Elsevier: Amsterdam, 1989.
(14) Hamzeh, F.; Bragg, R. *J. Appl. Phys.* **1974**, *45*, 3189.
(15) Wu, W. *J. Polym. Sci., B: Polym. Phys.* **1980**, *18*, 1659.
(16) Wignall, G.; Bates, F. *J. Appl. Crystallogr.* **1987**, *20*, 28.

MA9508111